Growing Gravity on Non-Linear Scales

Pablo Daniel Contreras Guerra

Supervisores: Dr. Carlos Hernández Moteagudo
Dr. Francisco-Shu Kitaura

Trabajo de Fin de Máster
presentado a la Universidad de La Laguna
en cumplimiento de los requerimentos del
Máster en Astrofísica

San Cristróbal de La Laguna, July 1, 2022

Dedicatoria

A mi familia. En especial a mis sobrinos, que con su visita y juegos hicieron que la escritura de este trabajo tome un poco más de tiempo del que debía, pero que ese tiempo lo llevaré siempre en el corazón. Los amo.

Resumen

Las surveys de galaxias que están en marcha y los futuros representan una era dorada para la investigación cosmológica y el estudio de la estructura a gran escala. Para poder extraer la información cosmológica de estos datos es necesario idear y probar observables sólidos y fiables. Recientemente, un nuevo observable basado en las fluctuaciones angulares de corrimiento al rojo, o redshift (ARF por su siglas en inglés), demostró ser sensible a los campos de materia y de velocidad peculiar. Además, este observable no muestra correlación con las fluctuaciones angulares de densidad de las galaxias (ADF) y es robusto frente a errores sistemáticos. Consecuentemente, es una herramienta promisoria para extraer información cosmológica de los surveys, como medir la tasa de crecimiento de estructuras determinado por las distorsiones en el espacio de redshift. Además, su caracter angular permite la comparación directa con predicciones teóricas. Sin embargo, la aplicabilidad de este observable se encuentra limitada a grandes escalas donde la teoría lineal, en la cual su formulación se basa, es válida. En este estudio se propone emplear reconstrucción cosmológica para ampliar la aplicabilidad de las ARF a escalas menores. La reconstrucción toma un campo evolucionado y deshace la gravedad para obtener el campo en una época evolutiva previa. Por tanto, el campo se linearizaría implicando una validez más amplia de las ARF. Esta idea se pone a prueba en catálogos simulados generados a partir condiciones iniciales emparejadas. Los catálogos fueron evolucionatos hasta un redshift de $z = 0.3$, y la reconstrucción se ejecutó hasta $z = 3.0$. A partir de la reconstrucción, el bias del catálogo respecto a un mismo redshift comóvil disminuye (de $b_1 = 1.32$ a $b_1 = 0.72$) indicando que el campo reconstruido es más sensible al campo de velocidades peculiares. El espectro de potencias de las ARF y ADF fue calculado para los catálogos antes y después de la reconstrucción. Estos fueron comparados con predicciones teóricas a partir de un modelo lineal obteniendo un buen acuerdo lo cual implica una buena determinación de parámetros, principalmente el bias pre y post reconstrucción. Finalmente, las ARF y ADF demostraron también ser más sensibles a la velocidad peculiar después de la reconstrucción. Esto demuestra la viabilidad de combinar ambas técnicas.

Abstract

Ongoing and upcoming galaxy surveys represent a golden era in cosmology and large scale structure research. In order to extract the cosmological information embedded in the data, strong and reliable observables need to be devised and tested. Recently, Angular Redshift Fluctuations (ARF) were proposed as a new observable that is sensitive to the matter density and peculiar velocity field, it also showed to be uncorrelated to the projected galaxy angular density fluctuations (ADF), and robust against systematic errors. Thus, it is a promising tool to extract cosmological information from surveys, such as measuring the growth rate of structures determined by the redshift space distortions. Furthermore, the angular character of the observable allows for direct comparison with theoretical predictions. However, its applicability is limited to large scales where linear clustering, in which its formulation is based, dominates. In this study, cosmological reconstruction is proposed to expand the applicability of ARF to smaller scales. As the name implies, reconstruction takes an evolved field and runs gravity back to obtain the field in a previous evolutionary epoch. Therefore, linearizing the field would imply a broader applicability of ARF. This idea is put to test on mock catalogues generated from a set of paired simulations evolved up to a redshift of $z = 0.3$, and the reconstruction was run up to $z = 3.0$. From reconstruction, the bias with respect to the same comoving redshift decreased (from $b_1 = 1.32$ to $b_1 = 0.72$) meaning that the post reconstruction field is more sensible to the peculiar velocity field. ARF and ADF power spectrum was calculated from the catalogues before and after the reconstruction and compared to theoretical predictions following a linear evolutionary model. These power spectra matched the theoretical predictions showing consistency and a good determination of the parameters such as pre and pos reconstruction bias. Finally, ARF and ADF also showed to be more sensible to the peculiar velocity after reconstruction. This demonstrates the feasibility of combining both techniques.

Contents

1. Introduction

Research on Cosmology and Large Scale Structure (LSS) of the Universe is currently in a golden era. Particularly, ongoing and upcoming galaxy surveys will yield a vast amount of data from which fundamental physics of the Universe can be explored. Such surveys map the positions and velocities of galaxies at different epochs and, from the first surveys, they show that the Universe is far from homogeneous but has a structure with over-dense (clusters) and sub-dense (voids) regions. However, when going to larger scales (> 100 Mpc), the Universe turns to be more homogeneous. It is at these larger scales that the Cosmological Principle, i.e. the universe is homogeneous and isotropic, is based. In simpler terms, this principle states that we are not in any special place in the universe.

Starting from this principle, models of the Universe and its evolution have been proposed and tested. The model widely accepted and able to describe very accurately the Universe is the so-called concordance or ΛCDM model. Such model tells that the universe is flat, expanding, and has transitioned from being dominated by radiation at its earliest stages, to subsequent matter domination with most of the matter being "dark" and "cold" (hence Cold Dark Matter, CDM), to be ultimately dominated by the so-called cosmological constant, Λ, or "dark energy", a component that accelerates the expansion. Although the model does well in describing the Universe and its evolution, it brings some problems lying on the unknown nature of Λ and CDM, and the evolution of structures under the action of gravity. Related to the latter, the generation of initial conditions that subsequently evolved into structures also posed a problem that was solved through the concept of inflation which consists of a rapid exponential expansion of the universe whose origin is not understood. Inflation also solved other problems rising from how the Cosmic Microwave Background (CMB) is homogeneous and isotropic, a problem connected to causality, and why the Universe is flat, a problem of fine tuning of cosmological parameters.

It is the problem of the evolution of structures under the action of gravity that this manuscript targets. In particular, the peculiar motions of galaxies, motions that deviate from the flow of expansion, are sensitive to the nature of gravity and galaxy surveys permit to massively study them as a function of cosmic history. Such peculiar motions cause distortions in the spatial distribution of galaxies in relation with their redshift, so-called redshift space distortions (RSDs).

Recently, a new technique to determine the growth rate, i.e. how fast density perturbations grow into full cosmological structures, based on angular fluctuations in the redshift space has been proposed. This technique has the advantage of being robust against systematics. Furthermore, its angular character allows direct comparison with theoretical predictions. It nevertheless suffers from one problem, its applicability is limited to large scales because it is sensible to the non-linear clustering of small scales. One potential solution to this problem lies in cosmological reconstruction. As the name implies, this consists of rolling back the motion of the galaxies, driven by gravity, to an earlier epoch of the Universe. Thus, reconstructing the galaxy distribution at that epoch which is more homogeneous. Having a more homogeneous distribution reduces the non-linear clustering and, therefore, can expand the applicability of angular redshift fluctuations (ARF) and angular density fluctuations (ADF) to smaller scales.

In this work, the latter idea is put to test with mock catalogues generated from cosmological simulations. Firstly, the theoretical background in which both techniques are based is explained in chapter 2. Then, the process to generate mock catalogues is pointed out in chapter 3 followed by the reconstruction implementation and the obtained ARF and ADF statistics in chapters 4 and 5, respectively. Finally, the concluding remarks and outlook are developed in chapter 6.

2. Theoretical Background

2.1 Standard Cosmological Model

The standard cosmological model, so called ΛCDM model, has been the most successful in explaining the formation of structures in the Universe. Its description includes a hot Big Bang origin, current domination of dark energy in the form of a cosmological constant, Λ, and the matter component dominated by the CDM. The model is supported and constrained observationally with the CMB, and with cosmic distance determination through type Ia supernovae and quasar spectra [1]. In the following, the basis and parameters of the standard model are described.

A homogeneous and isotropic Universe in the framework of general relativity (GR) can be described with the Friedmann-Lemaítre-Robertson-Walker (FLRW) metric,

$$ds^2 = -dt^2 + a^2(t)\left[\frac{dr^2}{1-kr^2} + r^2\left(d\theta^2 + \sin^2\theta d\phi^2\right)\right], \tag{2.1}$$

where t is the time coordinate, r, θ and ϕ are the spatial coordinates, $a(t)$ is the dimensionless scale factor, and k is the curvature constant defining the geometry of the Universe with $k < 0$, $k = 0$, and $k > 0$ corresponding to an open, flat and closed geometry, respectively. $a(t)$ is a monotonically increasing quantity and can be used to refer to different ages of the Universe, either past or future. Another parameter of interest is the cosmological redshift, defined as the amount that the wavelength of an emitted photon has stretched due background expansion. It is related to the scale factor, following

$$\frac{a_0}{a} = \frac{\lambda_{\text{obs}}}{\lambda_{\text{emit}}} = 1 + z. \tag{2.2}$$

The subscript 0 refers to the present day value, and for the scale factor is normalized to be unity $a_0 = a(t_0) = 1$.

Under the assumption of the cosmological principle, the smooth background can be described as a perfect fluid with density ρ and pressure p. Plugging the metric, and the stress-energy tensor

into the Einstein field equations leads to the Friedmann equations,

$$H^2(a) \equiv \left(\frac{\dot{a}}{a}\right)^2 = \frac{8\pi G}{3}\rho - \frac{k}{a^2} \tag{2.3}$$

$$\frac{\ddot{a}}{a} = -\frac{4\pi G}{3}(\rho + 3p). \tag{2.4}$$

$H(a) \equiv \dot{a}/a$ is the Hubble parameter and describes the expansion rate of the Universe. At present day, the parameter is denoted as H_0 and it is customary to express it in terms of the dimensionless Hubble parameter h, i.e. $H_0 = 100h$ km s^{-1} Mpc^{-1}.

Friedmann equations represent the energy and force balance of the universe. To complete these equations and solve the evolution of the scale factor, an equation of state is needed, together with the description of the components contributing to the total density. For each of the Universe's components the expression is $p = \omega\rho$, with ω a constant. Particularly, the values are $\omega = 0$ for non-relativistic collisionless matter, $\omega = 1/3$ for radiation, and $\omega = -1$ for cosmological constant. Plugging the equation of state into (2.4) reveals that a has an accelerated expansion when $\omega < -1/3$, defining a more general equation of state for the dark energy. Following energy conservation, the density evolution with the scale factor turns to be

$$\rho = a^{-3(1+\omega)}, \tag{2.5}$$

indicating that each component of the density evolves differently with time and there are epochs where one component dominates the total density over the others.

Density parameters are defined by normalizing each component density by the critical density, i.e. $\Omega_i(z) = \rho_i(z)/\rho_{\mathrm{crit}(z)}$. This critical value is the total density for a flat geometry, solving from equation (2.3)

$$\rho_{\mathrm{crit}} = \frac{3H^2}{8\pi G}. \tag{2.6}$$

Then a total density parameter is defined as the sum of all components parameters, i.e. $\Omega_{\mathrm{tot}} = \Omega_{\mathrm{m}} + \Omega_{\mathrm{r}} + \Omega_\Lambda$ for matter (including CDM and "normal" baryonic matter, $\Omega_{\mathrm{m}} = \Omega_{\mathrm{c}} + \Omega_{\mathrm{b}}$), radiation and cosmological constant (with energy density $\rho_\Lambda = \Lambda/8\pi G$). If the curvature density is introduced,

$$\rho_k = -\frac{3k}{8\pi G a^2} \tag{2.7}$$

equation (2.3) is simplified to $\sum \Omega_i + \Omega_k = \Omega_{\text{tot}} + \Omega_k = 1$. Expressing it in terms of present day parameters and remembering that $k = 0$ in the ΛCDM model, gives

$$H^2(z) = H_0^2 \left[\Omega_{\text{m},0}(1+z)^3 + \Omega_{\text{r},0}(1+z)^4 + \Omega_\Lambda \right]. \tag{2.8}$$

Equation (2.8) gives then a simpler expression for the evolution of the Hubble parameter based in present day values. This turns to be useful in determining comoving and angular cosmological distances, that in the ΛCDM model are expressed by*

$$D_c(z) = \int_0^z \frac{dz'}{H(z')}, \tag{2.9}$$

$$D_A(z) = \frac{D_c(z)}{1+z}. \tag{2.10}$$

Consequently, the standard ΛCDM model is described by a set of six parameters, seven if the null curvature is counted. Their values, as measured by the Planck Collaboration[2] are summed in the table 2.1. In this section h, $\Omega_{\text{b}}h^2$, $\Omega_{\text{c}}h^2$ where introduced. The following three, n_s, τ, and $\ln 10^{10} A_s$, are the primordial power spectrum index, reionization optical depth and the amplitude of primordial curvature perturbations, respectively.

Parameter	Description	Value
h	Dimensionless Hubble parameter	0.6774 ± 0.0046
$\Omega_{\text{b}}h^2$	Baryon density at present day	0.02230 ± 0.00014
$\Omega_{\text{c}}h^2$	CDM density at present day	0.1188 ± 0.0010
n_s	Primordial, scalar power spectrum index	0.9667 ± 0.0040
τ	Thomson scattering optical depth due reionization	0.066 ± 0.012
$\ln 10^{10} A_s$	Primordial curvature perturbations amplitude	3.064 ± 0.023

Table 2.1: The six fundamental parameters of the ΛCDM model as measured by the Planck Collaboration[2] (Table 4, column TT, TE, EE+lowP+lensing+ext). Further parameters of the model are derived from these.

*Note that the angular distance expression is only valid for a flat geometry.

2.2 Density Perturbations

A completely homogeneous Universe would not grow structures. Therefore, density fluctuations must be taken into account. The overdensity field, or density contrast, in configuration or real space is defined as,

$$\delta(\mathbf{x}) = \frac{\rho(\mathbf{x}) - \rho_0}{\rho_0} \tag{2.11}$$

with $\rho(\mathbf{x})$ the density at $\mathbf{x}$ and ρ_0 the mean density of some object of interest in the Universe. From Fourier expanding (2.11), its expression in terms of the wavenumber, $\delta(\mathbf{k})$, is obtained:

$$\delta(\mathbf{x}) = \sum_{\mathbf{k}} \delta_{\mathbf{k}} \mathrm{e}^{-i\mathbf{k}\cdot\mathbf{x}}. \tag{2.12}$$

However, a Fourier expansion of the density field in an infinite Universe is not well defined. Then, it needs to be assumed that the field is periodic within some box of volume $V = L^3$, restricting the allowed wavenumbers to harmonic boundary conditions, i.e. $k_i = 2\pi n_i/L$ for $i = x, y, z$.

The homogeneity of the Universe implies that the statistical properties of $\delta(\mathbf{x})$ should also be homogeneous. These can be studied via N-point correlators, $\langle \delta_1 \delta_2 \dots \delta_N \rangle$. Formally, $\langle \dots \rangle$ refers to an ensemble average. Nevertheless, there is only access to one realization of the ensemble, i.e. our Universe. This is solved by taking advantage of the ergodicity of Gaussian fields and replacing the ensemble average with a spatial one. Particularly, it is widely accepted that primordial density fluctuations were generated by the inflationary scenario that predicts the initial density fluctuations to be Gaussian[3,4]. Another characteristic of a Gaussian field is that its statistical properties are fully specified by the two-point statistics, i.e. correlation function in configuration space or the power spectrum in the Fourier space. The correlation function is defined as,

$$\xi(\mathbf{r}) \equiv \langle \delta(\mathbf{x}) \delta(\mathbf{x} + \mathbf{r}) \rangle. \tag{2.13}$$

It proves how density perturbations at different locations are correlated giving a positive result if both are over or under dense and negative if they are opposite. On the other hand, the power spectrum is a measure of the variance of density fluctuations at a given scale,

$$P(\mathbf{k}) = \langle |\delta_{\mathbf{k}}|^2 \rangle. \tag{2.14}$$

Actually, (2.13) and (2.14) are closely related, Fourier expanding the δ's in (2.13) gives

$$\xi(\mathbf{r}) = \left\langle \sum_{\mathbf{k}} \sum_{\mathbf{k}'} \delta_{\mathbf{k}} \delta_{\mathbf{k}'} e^{-i\mathbf{k}'\cdot\mathbf{x}} e^{-i\mathbf{k}(\mathbf{x}+\mathbf{r})} \right\rangle = \left\langle \sum_{\mathbf{k}} \sum_{\mathbf{k}'} \delta_{\mathbf{k}} \delta^*_{\mathbf{k}'} e^{i(\mathbf{k}'-\mathbf{k})\mathbf{x}} e^{-i\mathbf{k}\cdot\mathbf{r}} \right\rangle = \frac{V}{(2\pi)^3} \int d^3k \, |\delta_{\mathbf{k}}|^2 e^{-i\mathbf{k}\cdot\mathbf{r}}.$$

In the second step, one of the δ's was replaced by its complex conjugate, given that they are real, and for the third step, all cross terms ($\mathbf{k} \neq \mathbf{k}'$) average to zero because of the boundary conditions. Lastly, the final sum was expressed as an integral. Therefore, the correlation function is nothing more than the Fourier transform of the power spectrum. Additionally, from isotropy, the power spectrum and correlation function must also be isotropic, i.e. $\langle |\delta_{\mathbf{k}}|^2 \rangle = |\delta_k|^2$. Then, the angular part of the integral is immediate by noting that $\xi(r)$ is real, therefore $e^{-i\mathbf{k}\cdot\mathbf{r}} \to \cos(kr\cos\theta)$, and from $d^3k = k^2 \sin\theta dk d\theta d\phi$, the integral can be written as

$$\xi(r) = \frac{V}{(2\pi)^3} \int P(k) \frac{\sin kr}{kr} 4\pi k^2 dk. \tag{2.15}$$

Here, $\sin(kr)/kr$ is acting as a window function, modifying the density field. This is a convolution in the configuration space. There are other window functions widely used to filter out scales smaller than a certain one thus smoothing the field, such as the top-hat or the Gaussian window functions.

2.3 Linear Perturbation Theory

Large Scale Structure is interested in knowing the evolution of density perturbations, $\delta(\mathbf{x})$. At initial times, baryons and photons were coupled as a fluid until recombination epoch and after decoupling, baryons transitioned to behave as an ideal gas. Furthermore, CDM is believed to behave as a collisionless fluid. Consequently, fluid equations are the ideal framework to describe $\delta(\mathbf{k})$ evolution. Following a Newtonian approach, the corresponding equations are:

$$\text{Continuity equation}: \quad \frac{d_c\rho}{d_c t} + \rho \nabla_{\mathbf{r}} \cdot \mathbf{v} = 0, \tag{2.16}$$

$$\text{Euler equation}: \quad \frac{d_c\mathbf{v}}{d_c t} = -\nabla_{\mathbf{r}}\Phi - \frac{\nabla_{\mathbf{r}} P}{\rho}, \tag{2.17}$$

$$\text{Poisson equation}: \quad \nabla_{\mathbf{r}}{}^2\Phi = 4\pi G\rho. \tag{2.18}$$

with $\frac{d_c}{d_c t} = \left[\frac{\partial}{\partial t} + (\mathbf{v}\cdot\nabla_{\mathbf{r}})\right]$ being the convective derivative.

Continuity and Euler equations describe energy and momentum conservation, respectively. Poisson equation describes the gravitational potential induced by the density distribution. These equations are with respect to a physical coordinate system (**r**), it is convenient to account for the expansion transforming them to a comoving system (**x**). Noting that $\mathbf{r} = a\mathbf{x}$, the velocity becomes

$$\mathbf{v} = \dot{\mathbf{r}} = \dot{a}\mathbf{x} + a\dot{\mathbf{x}} = H\mathbf{r} + a\mathbf{u}, \tag{2.19}$$

where $\delta_{\mathbf{v}} = a\mathbf{u} = a\dot{\mathbf{x}}$ is the peculiar velocity. Consequently, the nabla operator transforms as $\nabla_{\mathbf{r}} = \nabla_{\mathbf{x}}/a$. Then, the convective derivative is,

$$\frac{d_c}{d_c t} = \frac{\partial}{\partial t} + (H\mathbf{r} + a\mathbf{u})\cdot\nabla_{\mathbf{r}} = \frac{\partial}{\partial t} + (H\mathbf{r}\cdot\nabla_{\mathbf{r}}) + (\mathbf{u}\cdot\nabla_{\mathbf{x}}) = \frac{d}{dt} + (\mathbf{u}\cdot\nabla_{\mathbf{x}}) \tag{2.20}$$

where $\frac{d}{dt} = \left[\frac{\partial}{\partial t} + (H\mathbf{r}\cdot\nabla_{\mathbf{r}})\right]$ is now the convective derivative but with respect to the comoving frame.

Plugging the transformations (2.19) and (2.20), adding perturbations about the homogeneous background ($\rho = \rho_0 + \delta_\rho = \rho_0(1+\delta)$, $P = P_0 + \delta_P$, and $\Phi = \Phi_0 + \delta_\Phi$), into the equations (2.16), (2.17), and (2.18), and keeping terms up to first order leads to the set of linearized fluid equations (demonstration in Appendix A):

$$\frac{d\delta}{dt} = -\nabla\cdot\mathbf{u}, \tag{2.21}$$

$$\frac{d\mathbf{u}}{dt} + 2H\mathbf{u} = -\frac{1}{a^2}\frac{\nabla\delta_P}{\rho_0} - \frac{1}{a^2}\nabla\delta_\Phi, \tag{2.22}$$

$$\nabla^2\delta_\Phi = 4\pi a^2 G\rho_0\delta. \tag{2.23}$$

Note that $\delta = \delta_\rho/\rho_0$ and that, although the equations are with respect to the comoving frame, the **x** subscript was omitted for simplicity.

An equation of state further simplifies one term. For an adiabatic expansion this is $c_s^2 = \partial P/\partial\rho$ and the pressure gradient term then becomes $\nabla\delta_P/\rho_0 = (\nabla\delta_\rho/\rho_0)(\nabla\delta_P/\nabla\delta_\rho) = (\partial\delta_P/\partial\delta_\rho)\nabla\delta = c_s^2\nabla\delta$. Taking the negative divergence on equation (2.22), and substituting equations (2.21) and (2.23) into the result leads to

$$-\frac{d}{dt}(\nabla\cdot\mathbf{u}) - 2H\nabla\cdot\mathbf{u} = \frac{c_s^2}{a^2}\nabla^2\delta + \frac{1}{a^2}\nabla^2\delta_\Phi \;\Rightarrow\; \ddot{\delta} + 2H\dot{\delta} = \frac{c_s^2}{a^2}\nabla^2\delta + 4\pi G\rho\delta. \tag{2.24}$$

Finally, Fourier expanding δ as in equation (2.12) allows to easily perform the substitution $\nabla \rightarrow -i\mathbf{k}$ in (2.24). This leads to an equation describing the evolution of the density perturbations amplitude:

$$\ddot{\delta}_{\mathbf{k}} + 2H\dot{\delta}_{\mathbf{k}} = \delta_{\mathbf{k}}\left(4\pi G\rho_0 - \frac{c_s^2 k^2}{a^2}\right). \tag{2.25}$$

Note that this equation applies for a non-relativistic fluid. Nevertheless, a similar approach leads to a similar expression for the relativistic case differing on the driving term factor at the r.h.s of the equation, i.e. $\ddot{\delta} + 2H\dot{\delta} = 32\pi/3G\rho_0\delta$. See Peacock [5] for reference.

Ignoring the second term in the l.h.s of (2.25), it is evident that when $4\pi G\rho_0 > c_s^2 k^2/a^2$ the perturbation grows exponentially. On the contrary, the pressure term dominates and the evolution is oscillatory, i.e. acoustic waves. This implies the existence of a limit scale given by $\lambda_J = c_s\sqrt{\pi/G\rho_0}$ separating both behaviours, this is called the Jeans length. Now, let's take the ignored term into account, and concentrate in scales much bigger than λ_J. For a matter (radiation) dominated Universe with $\Omega_{\mathrm{m}} = 1$ ($\Omega_{\mathrm{r}} = 1$). Noting that

$$\text{matter dominated } (a \propto t^{2/3}) : 4\pi G\rho_0 = \frac{2}{3t^2},$$
$$\text{radiation dominated } (a \propto t^{1/2}) : 32\pi G\rho_0/3 = \frac{1}{t^2}.$$

a power-law solution, i.e. $\delta \propto t^n$ is possible. There is no more exponential growth, therefore this term, accounting for the Hubble expansion, acts as a drag force. The solution for matter domination is $n = 2/3$ and $n = -1$ while for radiation domination $n = \pm 1$. This defines a growing and a decaying mode, denoting a general solution[†] of the form

$$\delta(t, \mathbf{k}) = \delta_{\mathbf{k},+}D_+(t) + \delta_{\mathbf{k},-}D_-(t). \tag{2.26}$$

Here, $D_+(t)$ is the growth function or factor. The decaying factor, $D_-(t)$, does not grow structure and can be ignored so that it is safe to just denote $D_+(t) = D(t)$. This factor is normalized to unity at present day value, i.e. $D(t_0) = 1$.

An alternative way to look at the growing solution is to look for solutions in the form $\mathbf{u} = -F(t)\frac{\nabla\delta_\Phi}{a} = F(t)\mathbf{g}$, with $\mathbf{g} = -\frac{\nabla\delta_\Phi}{a}$ the peculiar gravitational acceleration. From equation (2.21) it follows that (See Appendix A for details)

$$\delta_{\mathbf{v}} = a\mathbf{u} = \frac{2f(\Omega)}{3H\Omega}\mathbf{g}, \tag{2.27}$$

[†]For the expressions in the general case, refer to Peacock [5].

where $f(\Omega) = (a/\delta)(d\delta/da) = d\ln\delta/d\ln a$ is the growth rate. An approximation for this is $f \approx \Omega^{0.6}$ given by Peebles[6]. Additionally, from Fourier expanding equation (2.23), i.e. $\delta_\Phi \propto \exp(-i\mathbf{k}\cdot\mathbf{x})$, and plugging in equation (2.27),

$$\delta_\mathbf{v} = -\frac{i\mathbf{k}}{k^2} f a H \delta. \tag{2.28}$$

This last equation implies that mapping the density and velocity fields gives a way of measuring Ω through the growth rate function $f(\Omega)$.

2.4 Zel'dovich Approximation

The treatment and evolution from §2.3 is valid only on linear scales when $\delta \ll 1$. Zel'dovich[7] formulated a kinematical approach applicable to non-linear evolution and formation of structures, up to some degree. It works out the initial displacement of a particle and assumes that it will continue to move in the same initial direction. In terms of Lagrangian coordinates $\mathbf{q}$, the real space coordinate is

$$\mathbf{r} = \mathbf{q} + \mathbf{\Psi}(\mathbf{q}, t) = \mathbf{q} + D(t)\psi(\mathbf{q}). \tag{2.29}$$

Then, at initial time, $\mathbf{r} = \mathbf{q}$ and the first term expresses the Hubble expansion. The second term is a perturbation over the expansion where $D(t)$ scales the time-independent displacement field $\psi(\mathbf{q})$. Here, $\mathbf{\Psi}(\mathbf{q}, t) \simeq D(t)\psi(\mathbf{q})$ comes from truncating the perturbative solution for the displacement field at first order in the formalism of Lagrangian Perturbation Theory, i.e. $\mathbf{\Psi} = \mathbf{\Psi}^{(1)} + \mathbf{\Psi}^{(2)} + \mathbf{\Psi}^{(3)} + \cdots$. From equation (2.22) it derives that pertubations are irrotational (see Appendix A for demonstration) and, thus, the displacement field can be written as a gradient of a scalar function, i.e. $\psi(\mathbf{q}) = \nabla\phi$. Now, from mass conservation, $\rho(\mathbf{r}, t)d^3x = \rho(\mathbf{q})d^3q$ and noting that $\rho(\mathbf{r}, t) = \rho_0 + \delta_\rho(\mathbf{r}, t)$ and $\rho(\mathbf{q}) = \rho_0$, it follows that

$$1 + \delta(\mathbf{r}, t) = J(\mathbf{q})^{-1} = \left|\frac{d^3r}{d^3q}\right|^{-1} = \left|\delta_{ij} + D(t)\frac{\partial\psi_i}{\partial q_j}\right|^{-1} = \left|\delta_{ij} + D(t)\frac{\partial^2\phi}{\partial q_i \partial q_j}\right|^{-1}, \tag{2.30}$$

where equations (2.29) and $\psi(\mathbf{q}) = \nabla\phi$ were used. The term $\partial^2\phi/\partial q_i\partial q_j$ defines a symmetric deformation tensor, which can be diagonalized leading to the solution in terms of its eigenvalues $\lambda_{1,2,3}(\mathbf{q})$

$$1 + \delta(\mathbf{r}, t) = \left[(1 - D(t)\lambda_1(\mathbf{q}))\,(1 - D(t)\lambda_2(\mathbf{q}))\,(1 - D(t)\lambda_3(\mathbf{q}))\right]^{-1} \simeq 1 + D(t)\delta_L(\mathbf{q}). \tag{2.31}$$

For the last step, the equation was linearized allowing to define the linear density field in Lagrangian coordinates, $\delta_L(\mathbf{q}) = \lambda_1(\mathbf{q}) + \lambda_2(\mathbf{q}) + \lambda_3(\mathbf{q})$. Similarly, linearizing equation (2.30) leads to the Zel'dovich approximation:

$$\delta = -D(t)\nabla \cdot \psi(\mathbf{q}) = -D(t)\nabla^2\phi(\mathbf{q}). \tag{2.32}$$

Finally, the displacement field is related to the linear velocity field via $\mathbf{v}(\mathbf{r}) = faH\psi(\mathbf{r})$, then in Fourier space and from equation (2.28)

$$\psi(\mathbf{k}) = -i\frac{\mathbf{k}}{k^2}\delta_{\mathbf{k}}. \tag{2.33}$$

indicating that the displacement field can be obtained from mapping the matter density field.

2.5 Initial Conditions and Transfer Function

Soon after the Big Bang, inflation stretched out quantum fluctuations to form the initial density perturbations that seeded cosmic structure formation. The predictions following inflation for the initial conditions are that the initial density perturbations were Gaussian and adiabatic, fully described by their power spectrum. Such primordial spectrum is nearly scale invariant and described as a power-law

$$P(k) = A_s k^{n_s}. \tag{2.34}$$

Scale invariant translates to $n_s = 1$, such power spectrum is known as the Harrison-Zel'dovich power spectrum. Table 2.1 shows the constrain in this parameter from the Planck Collaboration, showing a very close agreement with a scale invariant spectrum.

The subsequent evolution of the density perturbations is much more complicated than what is introduced in §2.3 and §2.4 requiring perturbative solutions for the Einstein equations and metric. However, a qualitative description can be sought. After inflation, the Universe expanded increasing the size of the comoving horizon, i.e. the limit denoting causally connected regions. Therefore, higher scale fluctuations keep on entering the horizon and modes inside the horizon can evolve with time. Such evolution depends on the component dominating the Universe, for radiation domination the growth is impeded by the radiation pressure while for matter domination fluctuations can grow more substantially. This denotes a characteristic scale for this evolution,

at the radiation-matter equality, $k = k_{\rm eq}$. Fluctuations with $k > k_{\rm eq}$ had their growth impeded because they entered the horizon before radiation-matter equality. Fluctuations with $k < k_{\rm eq}$, on the other hand, could grow soon after they entered the horizon. This denotes a turnover in the power spectrum at $k_{\rm eq}$. This evolution is encoded in the transfer function, $T(k)$, that transforms the primordial power spectrum to the power spectrum of evolved perturbations,

$$P(k, z) \propto \sigma_8^2 D^2(z) T^2(k) k^{n_s}. \tag{2.35}$$

The transfer function is a time-independent factor so that the time evolution is encoded in the growth function. The normalization of the power spectrum is given by σ_8 that expresses the variance of density fluctuations today smoothed to a comoving scale of 8 h^{-1} Mpc. Analytic approximations do exist for $T(k)$, for instance the one from Eisenstein *et al.* [8], however there are also numerical solutions that solve the set of Einstein and Boltzmann equations, CAMB [9] and CLASS [10] being widely used codes. It is useful to see the asymptotic behaviour,

$$T(k) \propto \begin{cases} 1 & \text{if} \quad k \ll k_{\rm eq}, \\ k^{-2} \ln k & \text{if} \quad k \gg k_{\rm eq}, \end{cases} \tag{2.36}$$

meaning that scale dependence of the evolved power spectrum in large scales, i.e. small k, mimics the one of the primordial spectrum.

2.6 Bias

Luminous matter in the universe, e.g. galaxies, does not represent the underlying matter density field but acts as a biased tracer of it. Then, to take advantage of the information encoded in the Large Structure of the Universe, it is fundamental to understand the relation between both density distributions. The bias parameter expresses this relation; in a general form, the bias is a functional of the matter density field [11],

$$\delta_g(\mathbf{x}) = F[\delta(\mathbf{x}')] \tag{2.37}$$

with δ_g being the density field of the tracer. In principle, $\mathbf{x} = \mathbf{x}'$ is not necessary and the relationship can be non-local. However, a common simplifying assumption is that the relationship is linear

in sufficiently large scales giving $\delta_g = b_1\delta$. Therefore, the two-point statistics are boosted by a constant factor,

$$\xi_g(r) = b_1^2\xi(r); \quad P_g(k) = b_1^2 P(k). \tag{2.38}$$

This simplification obviously breaks down at small scales, where non-locality and non-linearity becomes important. Furthermore, the bias of a tracer, e.g. galaxies, can depend on the different morphological types of the tracer. Discrete objects also contribute a level of stochasticity to the tracer, ruling out this simplification. For the interests of this study, the linear assumption is sufficient and will be used.

2.7 Redshift Space Distortions

Surveys do not look at the Universe in the configuration or real space, instead, they look in the redshift space, where the radial direction is distorted. In fact, the third dimension, i.e. the redshift, is not only sensible to the Hubble flow but also to the peculiar velocity field and does not represent correctly the radial distance to objects. Actually, this distance is distorted leading to the so-called Redshift Space Distortions (RSDs). On larger, i.e. linear, scales, objects fall into overdensities, the ones on the side of the overdensity closer to the observer look farther while the ones on the opposite side of it look closer. This results in an overall squashing effect, enhancing the overdensity and is sourced by a coherent component of the peculiar velocity field. On the smaller, i.e. non linear, scales, objects have random motion, from the dispersed component of the peculiar velocity field, and two objects at the same distance will have slightly different redshift. In result, the structures appear elongated along the line of sight of the observer forming the so-called Fingers-of-God. Consequently, the power spectrum is enhanced at larger scales and the opposite happening at smaller scales. An schematic of these effects is depicted in figure 2.1. Since the peculiar velocity field is sourced by the gravitational potential, clustering in redshift space contains an anisotropic signal with cosmological information about the growth rate of the Universe.

RSDs where first fully described in Kaiser[12], the transformation from coordinates in real space, $\mathbf{r}$, to coordinates in redshift space, $\mathbf{s}$, is given by

$$\mathbf{s} = \mathbf{r} + \mathbf{v}_r = \mathbf{r} + \frac{\mathbf{u}\cdot\hat{\mathbf{r}}}{aH}\hat{\mathbf{r}}. \tag{2.39}$$

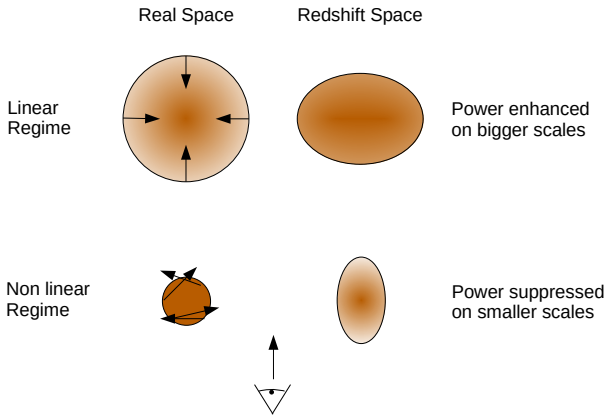

Figure 2.1: Redshift Space Distortions effect on large and small scales.

Note that the factor $1/aH$ serves to conciliate units of the peculiar velocity field, $\mathbf{v}_r$, to units of length. Additionally, $u_{\rm los} = \mathbf{u} \cdot \hat{\mathbf{r}}$ is the peculiar velocity along the line of sight. Here, the peculiar velocity of the observer is assumed to be null. The Jacobian, under the assumption of a distant observer so that second order terms vanish, is

$$\frac{d^3 s}{d^3 r} = \left(1 + \frac{1}{aH}\frac{du_{\rm los}}{dr}\right). \tag{2.40}$$

The second term in the r.h.s. can be further solved, noting a Fourier expansion, as

$$\frac{1}{aH}\frac{du_{\rm los}}{dr} = \frac{\mu}{aH}\frac{du}{dr} = \frac{\mu}{aH}(-ik\mu u) = \frac{\mu^2}{ah}\frac{(ik)^2}{k^2} faH\delta = (-\mu^2 f\delta),$$

where equation (2.28) was used and $\mu = \hat{\mathbf{k}} \cdot \hat{\mathbf{r}}$. Also, noting that, $\dot{\delta} = iku$ (from equation (2.21)), from the last steps above $\dot{\delta} = faH\delta$ is also derived. Now, from mass conservation it is evident that $\delta_s d^3 s = \delta d^3 r$. Plugging everything together leads to

$$\delta_s = (1 + f\mu^2)\delta. \tag{2.41}$$

Furthermore, taking a biased tracer, $\delta_g = b_1\delta$, the relation between tracer's power spectrum in redshift space and matter power spectrum in real space is derived from equation (2.41):

$$P_g^s(k,\mu) = \left[1 + \beta\mu^2\right]^2 b_1^2 P(k). \tag{2.42}$$

Here, $\beta \equiv f/b_1$ is defined as the linear RSD factor. Lastly, the expansion of (2.42) into Legendre polynomials, $\mathcal{L}_\ell$, is

$$P_g^s(k,\mu) = \sum_{\ell=0,2,4} P_\ell(k)\mathcal{L}_\ell(\mu) = P_0(k)\mathcal{L}_0(\mu) + P_2(k)\mathcal{L}_2(\mu) + P_4(k)\mathcal{L}_4(\mu), \tag{2.43}$$

meaning that linear RSDs can be fully described by the monopole ($\ell = 0$), quadrupole ($\ell = 2$), and hexadecapole ($\ell = 4$) multipoles. It is important to remark that measuring β and modeling RSDs constrain the growth of structure in the Large Scale Structure.

2.8 Angular Redshift Fluctuations & Angular Density Fluctuations

On basis of extracting the cosmological information included in RSDs, a new observable was proposed by Hernández-Monteagudo *et al.* [13]. This observable, the Angular Redshift Fluctuations (ARF), is based on the estimation of the average redshift of all galaxies on a given sky position/sky pixel in an observation. The galaxies are assigned a Gaussian weight of the form

$$W_j \equiv \exp\left(-\frac{(z_j - z_{\rm obs})^2}{2\sigma_z^2}\right), \tag{2.44}$$

with z_j the observed redshift of the j-th galaxy, and $z_{\rm obs}$ and σ_z^2 the chosen central redshift and redshift width for the Gaussian kernel, respectively. On this basis, the ARF is computed like

$$\delta z(\hat{n}) = \frac{\sum_{j\in\hat{n}} W_j(z_j - \bar{z})}{\langle \sum_{j\in\hat{n}} W_j \rangle_{\hat{n}}}. \tag{2.45}$$

Here, the numerator sum is over all galaxies into the pixel at $\hat{n}$, $\bar{z} = (\sum_j W_j z_j)/(\sum_j W_j)$ is the average redshift of the sample in the entire footprint of the survey, and $\langle \dots \rangle_n$ denotes the angular average over the same footprint. Particularly, the ARF field is shown to be sensitive to both matter and radial velocity fields

$$\bar{z} + \delta z(\hat{n}) = \mathcal{F}[z_H] + \mathcal{F}\left[b_g \delta(z_H - \mathcal{F}[z_H])\right] + \mathcal{F}\left[\frac{\mathbf{u}\cdot\hat{\mathbf{n}}}{c}(1+z_H)\left(1 - \frac{d\ln W}{dz}(z_H - \mathcal{F}[z_H])\right)\right] + O(2^{\rm nd}), \tag{2.46}$$

with b_g the galaxy bias, z_H the redshift correspondent to the Hubble flow, and $\mathbf{u}$ the peculiar velocity. Additionally, the kernel $\mathcal{F}[g]$ denotes the normalized integral of a function g under the Gaussian redshift window

$$\mathcal{F}[Y] = \frac{\int dr r^2 \bar{n}(r) W(z_H, \sigma_z) Y(r)}{\int dr r^2 \bar{n}(r) W(z_H, \sigma_z)} = \frac{1}{\mathcal{N}} \int dr r^2 \bar{n}(r) W(z_H, \sigma_z) Y(r).$$

Particularly, if the matter density or line of sight peculiar velocity are constant under the window, they do not contribute to the ARF. Additionally, with small values of σ_z the kernels turn to be orthogonal to the corresponding kernels of the number angular density fluctuations (ADF), i.e. 2D angular clustering, defined by

$$\delta_g(\hat{n}) = \mathcal{F}[b_g \delta] + \mathcal{F}\left[\frac{\mathbf{u}\cdot\hat{\mathbf{n}}}{c}(1+z_H)\frac{d\ln W}{dz}\right] + O(2^{\text{nd}}). \tag{2.47}$$

Therefore, ARF and ADF provide complementary information to each other. Interestingly, ARF are highly correlated to the line of sight peculiar velocities allowing to characterize them and combine with other observables for the peculiar velocity field. Furthermore, ARF are little sensitive to systematics with the biasing being cancelled by the ADF. Then, these observables constitute a very interesting tool to extract cosmological information from surveys, carrying additional information to that of 2D angular clustering.

The angular power spectrum, i.e. $\langle \delta(\mathbf{n})\delta(\mathbf{n}+\theta)\rangle_{\mathbf{n}} = C(\theta) = \sum_\ell \frac{2\ell+1}{4\pi} C_\ell P_\ell(\cos\theta)$, can be computed for both ARF and ADF. And it is shown to be given by[‡]

$$C_\ell^{\delta z,\delta z} = b_g^2 C_\ell^{\delta,\delta} + 2 b_g C_\ell^{\delta,u_{\text{los}}} + C_\ell^{u_{\text{los}},u_{\text{los}}}, \tag{2.48}$$

having a density term, a line of sight velocity term and a cross term. Particularly, these spectra are sensitive to the cosmological parameters $b_g\sigma_8(z)$, from the density term, and $E(z)f(z)\sigma_8(z)$, from the line of sight velocity term; note that $E(z) \equiv H(z)/H_0$. Finally, it is worth to state that these observables are based on the assumption of galaxies being a linear tracer of the matter field, i.e. equation (2.38). Therefore, their applicability is somewhat limited to big, linear, scales where this assumption is correct. Nevertheless, this represents a chance to combine these observables with additional techniques and take advantage of them in non-linear scales.

[‡]For the detailed expressions of the factors $C_\ell^{\alpha,\beta}$ and $\Delta_\ell^\alpha(k)$ refer to Hernández-Monteagudo *et al.* [13].

3. Generation of Mock Catalogues

In this section, the followed process to generate catalogues of mock data will be described. The catalogues were built and analyzed using state-of-the-art LSS algorithms, some implemented through the **nbodykit**[14] toolkit. This tooolkit is written in Python, and therefore, the hard coded procedures in the generation and analysis of the datasets were also written in Python. Additionally, it is important to note that the cosmology used in the whole workflow comes from the last results from the Plank collaboration[2]. Its main parameters are summarized in the table 2.1.

3.1 Paired Simulations

Cosmological simulations have the limitation of a sparse sampling of Fourier modes due to the limited size of the box. This results on a poor sampling to the largest modes and implies a limit on the inferences that can be made based on the simulations[15]. This is closely connected to the cosmic variance, i.e. due to the limited volume covered by surveys there is an irreducible source of error, that in the computational case can be suppressed until it is smaller than its observational counterpart. This is done by simulating a large number of realizations implying a huge computational cost. As an alternative, Angulo and Pontzen[15] proposed a method that effectively suppresses the box variance with only two simulations that are paired to each other achieving the accuracy from a large number of simulations.

The paired simulations are based on the generation of the initial conditions (ICs) density field. First, an initial realization of a Gaussian density field, δ_G, based on the linear power spectrum P_L is performed. This power spectrum is the primordial one evolved to a desired redshift through the transfer function, as in equation (2.35). Then the ICs for the paired simulations are defined following

$$\hat{\delta}(\mathbf{k}) = \sqrt{\frac{P_L(k)}{P_{\delta_G}(\mathbf{k})}}\delta_G(\mathbf{k}), \tag{3.1}$$

where $P_{\delta_G}(\mathbf{k}) = \Re[\delta_G(\mathbf{k})]^2 + \Im[\delta_G(\mathbf{k})]^2$ is the three dimensional power spectrum of the Gaussian

field. Then, the two ICs are set by the inverse Fourier transform and its negative:

$$\hat{\delta}_1(\mathbf{r}) = \mathrm{IFT}[\hat{\delta}(\mathbf{k})]; \qquad \hat{\delta}_2(\mathbf{r}) = -\mathrm{IFT}[\hat{\delta}(\mathbf{k})]. \tag{3.2}$$

This way, the two simulations use a fixed power spectrum equal to the one of the Gaussian realization, and are paired meaning that chance phase correlations can be cancelled.

After generating the ICs, the workflow to generate the simulations is:

1. **Convolution of ICs:** A further modification needs to be included in the ICs in order to seed non linearity into the input power spectrum. This, as done in the **EZmocks**[16] code, allows to model non linear clustering at two point statistics level. The ICs are convolved with a kernel in the following form

$$\delta_{\mathrm{NL}} = \sqrt{\frac{P_{NL}(k)}{P_L(k)}} \circledast \delta_L, \tag{3.3}$$

   with δ_L being each of the linear paired ICs density field and $P_{NL}(k)$ is the non-linear power spectrum which can be retrieved from a theoretical model including non-linear evolution or from an N-body simulation evolved field. In this case, the latter was used since simulation trials were at disposal.

2. **Forward Zel'dovich evolution:** From the convolved ICs field, the displacement field can be calculated following equation 2.33. Starting from a mesh of uniformly distributed particles, the displacement field is interpolated to each particle and the corresponding displacement is applied to the particles. Consequently, new particle positions are obtained defining the evolved matter density field δ.

3. **Deterministic bias application:** Tracers (e.g. galaxy or halos) are related to the underlying matter field through a non-linear, non-local and stochastic relation[17,18]. To account for the non-linearity, a deterministic bias can be applied to the matter density field. This follows the procedure described in the **PATCHY** code[19], where, neglecting non-local biasing, the expected number of tracers in a cell i of the density field is

$$\lambda_i = \langle N_i \rangle = \gamma\theta(\delta_{th})(1 + \delta_i)^{\alpha}. \tag{3.4}$$

Here α controls the bias while γ controls the number density. $\theta(\delta_{th})$ is a step function based on a overdensity threshold δ_{th} so that if the cell overdensity is higher, it can host galaxies. In the opposite case, the cell will be empty.

4. **Stochastic bias application:** On the other hand, to account for the stochastic bias, a Poisson realization of the expected number of tracer in the cell is performed, i.e. $P(N_i|\lambda_i) = (\lambda_i^{N_i}/N_i!)\exp(-\lambda_i)$. This way, obtaining the number of galaxies for the cell i.

5. **Build galaxy catalogue:** For each of the N_i galaxies determined for each cell, a random position inside the cell is applied. The random position is determined by a realization of a uniform distribution.

6. **Add RSDs to the catalogue:** Lastly, to simulate a real survey it is needed to move the tracers position from the real space to the redshift space by applying the RSDs corresponding to the peculiar velocity field, i.e. equation (2.39). The peculiar velocity field is comprised of a coherent, leading to the large scale squashing effect, and a disperse, leading to the small scale Fingers-of-God effect, components. Particularly, the coherent component is proportional to the displacement field via equations (2.28) and (2.33). Therefore, from the matter field δ the displacement field can be extracted, multiplied by a fiducial growth rate, and projected to the line of sight unit vector defined by the observer position in the box[20].

At the end of each simulation, two catalogues are obtained corresponding to the matter and galaxies position and distribution.

3.2 Mock catalogue description

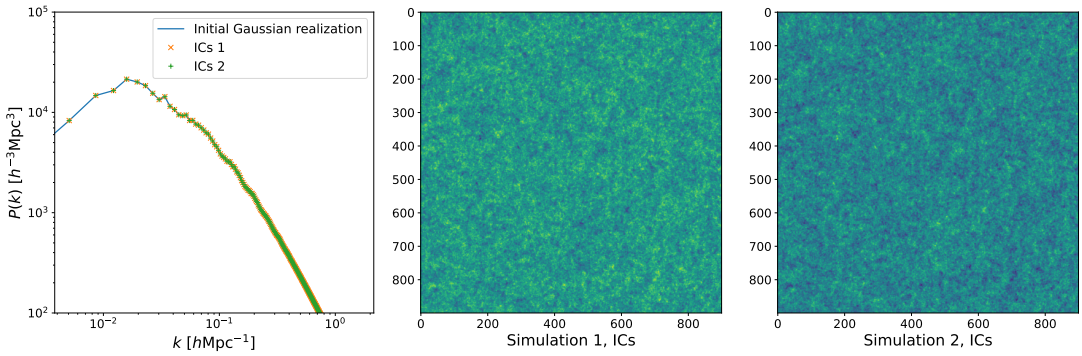

Figure 3.1: Power spectrum and density fields of the paired set of initial conditions. Note that the power spectrum of each field is equal to the initial Gaussian realization and their opposite nature in the over(under) densities corresponding to under(over) densities on the other field.

The target redshift of the linear power spectrum was set to $z = 0.3$. Then, the box size should be a comoving distance of $L = 1755$ Mpc h^{-1} when placing the observer at the center of the box, that is, to reach the same redshift when converting from cartesian to celestial coordinates given the chosen cosmology. The mesh resolution is set to $N_c = 900$ cells per dimension.For the deterministic bias application, the parameters are set to $\alpha = 1.3$, $\delta_{th} = 0$, and $\gamma = 0.02$. These parameters showed to be the best to obtain an ELG survey-like catalogue. The galaxy number density for the paired simulations is $3.5 \times 10^{-3} h^3$ Mpc^{-3}.

The ICs paired fields and their power spectra can be seen in the figure 3.1. Particularly, it can be verified the opposite nature of the fields and their fixed power spectrum with respect to the Gaussian realization, something expected by construction.

From the matter and galaxy catalogues the power spectrum can be extracted and compared, this is illustrated in the figure 3.2. As expected, the matter power spectrum $P(k)$ and the ICs one are the same at the largest scales (small k), only differing at the smallest ones (large k). The galaxy power spectrum $P_g(k)$ is higher in power as expected to, due the bias of the tracer. The

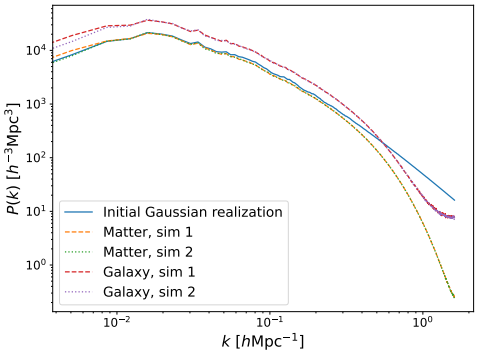

Figure 3.2: Power spectrum of the ICs, matter field and halos field from the paired simulations.

bias of the galaxy catalogue can be computed, from modifying the equation (2.38)

$$b_1 = \sqrt{\left\langle \frac{P_g(k)}{P(k)}\bigg|_{\text{low } k} \right\rangle} \Rightarrow b_{1,\text{sim 1}} = b_{1,\text{sim 2}} = 1.32, \tag{3.5}$$

where the low k limit is due to the validity of the linear bias approximation to large, linear scales, and $\langle \dots \rangle$ is a normal average. The chosen range in k cannot be too low neither, to avoid cosmic variance. In particular, plotting $\sqrt{P_g(k)/P(k)}$ allows to define the range where the linear bias applies and where the cosmic variance does not dominate, this is shown in the figure 3.3. Based on this, the chosen range to evaluate the bias is $0.03 \leq k \leq 0.09$, giving the results in equation (3.5). This bias is similar to ELG galaxies*, as explained before, this was expected from the parameters of the deterministic bias application.

Finally, the distribution in real and redshift space can be compared as shown in the figure 3.4 with both the density field and power spectra. Particularly, giving that only the coherent component is being simulated, the overall effect of RSDs is to enhance the power, i.e. squashing effect in §2.7, as shown in both density field and power spectrum. This can be seen in the more clumpy distribution of the density field in redshift space in the figure.

*For instance, see Zhai *et al.* [21].

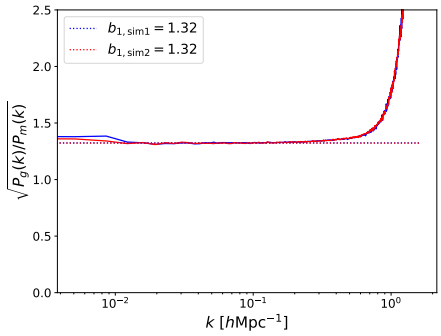

Figure 3.3: Square root of the ratio between tracer and matter power spectrum, at $k \lesssim 0.03$ cosmic variance dominates and at $k \gtrsim 0.09$ the linear bias approximation loses validity.

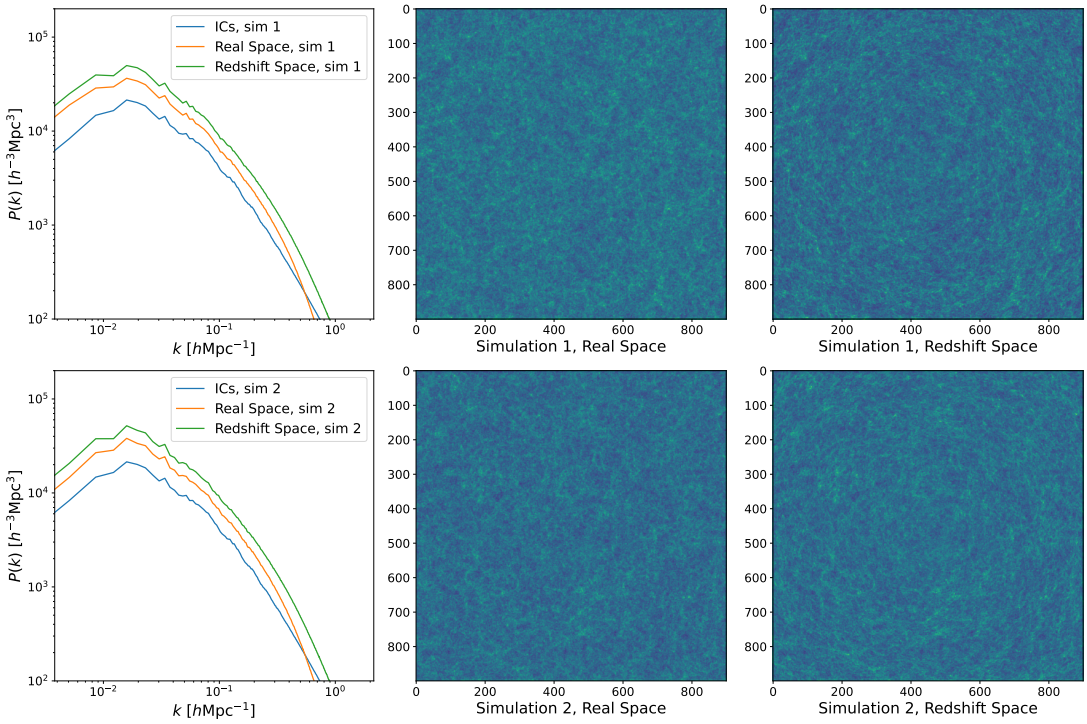

Figure 3.4: Effect of RSDs over the halos distribution. In general, the squashing effect is prominent as can be verified in both the power spectrum and density fields.

4. Reconstruction

Galaxy surveys look at an evolved state of the universe. At such state, non-linear evolution of structures dominates making it difficult to extract cosmological information given that the theories are better confronted to earlier epochs of the universe with a more homogeneous distribution. One example of this statement is the measurement of the Baryon Acoustic Oscillation (BAO) peak in the correlation function which is broadened due to non-linear gravitational structure formation and RSDs[22]. However, Eisenstein *et al.*[23] showed that the peak is restored after applying reconstruction, i.e. from the density field obtain the linear theory displacement field and move the particles/galaxies in the opposite direction. As stated in §2.8, the determination of the growth rate through ARF is limited to the large scales because it is sensible to non-linear clustering. Then, in the interest of this study, reconstruction can be implemented in order to improve the growth rate determination and expand its applicability towards smaller scales. In this section, the reconstruction process and how it was implemented will be explained as well as some tests performed in order to check the correctness of its application.

4.1 Implementation

Combining equations (2.29) and (2.39), the redshift space coordinate in terms of the Lagrangian coordinate at a given redshift, is

$$\mathbf{s}(z) = \mathbf{q} + \mathbf{\Psi}(\mathbf{q}, z) + \mathbf{v}_r(\mathbf{r}(\mathbf{q})) = \mathbf{q} + D(z)\psi(\mathbf{q}) + \mathbf{v}_r(\mathbf{q}), \tag{4.1}$$

thus, the Lagrangian coordinate is solved as $\mathbf{q} = \mathbf{s}(z) - D(z)\psi(\mathbf{q}) - \mathbf{v}_r(\mathbf{q})$. However, inferring $\mathbf{q}$ turns to be a difficult task since it is needed to have prior knowledge of the density field and peculiar velocity field, which depend on $\mathbf{q}$, as explained by Kitaura *et al.*[24].

If the positions of some tracers and their density field at an earlier redshift z_{high} wants to be known from the positions and density field at a later, or observed, redshift z_{low} one can substract the Lagrangian coordinate in terms of z_{low} in the expression (4.1) at z_{high} giving

$$\mathbf{s}(z_{\text{high}}) = \mathbf{s}(z_{\text{low}}) - (D(z_{\text{low}}) - D(z_{\text{high}}))\psi(\mathbf{q}). \tag{4.2}$$

Algorithm 1 Iterative Reconstruction

$i \leftarrow 0$
$\mathbf{q} \leftarrow \mathbf{s}$
while $(i < N_{\text{iter}})$ **do**
  $\mathbf{q}' \leftarrow \mathbf{s} - (D(z_{\text{low}}) - D(z_{\text{high}}))\psi(\mathbf{q}) - \mathbf{v}_r(\mathbf{q})$
  $\mathbf{q} \leftarrow \mathbf{q}'$
  $i \leftarrow i + 1$
end while
$\mathbf{qs} \leftarrow \mathbf{s} - (D(z_{\text{low}}) - D(z_{\text{high}}))\psi(\mathbf{q})$

Note that the peculiar velocity field gets cancelled by this operation. Equation (4.2) represents the basic formulation of the reconstruction scheme to be used in this work. However, the displacement field is defined from the matter distribution in Lagrangian coordinates, i.e. equation (2.33), and prior to applying the reconstruction, the only information available is the distribution of the tracer at redshift space. Then, it is needed to estimate the displacement field in base of this information. Recalling the bias relation between the matter and tracer density fields, $\delta_g = b_1\delta$, the matter density field is estimated by dividing the tracer density field by the bias. Additionally, the field is smoothed to filter out the small scales corrupted by nonlinearities[22]. The filter consists of a Gaussian filter, defined as $W_R(\mathbf{k}) \equiv \exp\left(-\frac{1}{2}k^2R^2\right)$ in Fourier space, with a characteristic radius so that smaller scales than R get smoothed. Therefore, the displacement field is estimated from the distribution of the tracer in redshift space as

$$\psi^{\mathbf{s}}(\mathbf{k}) = -i\frac{\mathbf{k}}{k^2}W_R(\mathbf{k})\frac{\delta_g^s(\mathbf{k})}{b_1} \Rightarrow \psi(\mathbf{s}) = \text{IFT}\left[\psi^{\mathbf{s}}(\mathbf{k})\right], \tag{4.3}$$

In a similar way, $\mathbf{v}_r(\mathbf{q})$ can be estimated from the tracer density field given that the linear RSDs arise from the displacement field as $f(\Omega)(\psi(\mathbf{s}) \cdot \hat{\mathbf{s}})\hat{\mathbf{s}}$ (with $\hat{\mathbf{s}}$ the radial direction in redshift space)[20,25,26], obtaining $\mathbf{v}_r(\mathbf{s})$. Finally, the Lagrangian coordinate is estimated as

$$\mathbf{q}' = \mathbf{s}(z_{\text{low}}) - (D(z_{\text{low}}) - D(z_{\text{high}}))\psi(\mathbf{s}) - \mathbf{v}_r(\mathbf{s}), \tag{4.4}$$

and with the estimated coordinates $\mathbf{q}'$ the displacement field can again be computed to perform the reconstruction in equation (4.2).

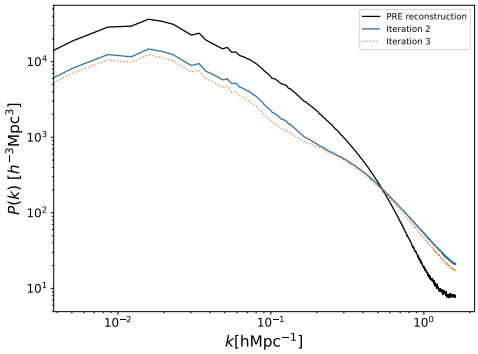

Figure 4.1: Iterative reconstruction at the third iteration. The pre reconstruction power spectrum used for reference is the one corresponding to real space.

To improve the accuracy in estimating $\mathbf{q}'$, an iterative reconstruction can be implemented[24,26]. This consists of the application of equation (4.4), updating $\mathbf{q}$ at each iteration to later apply the equation (4.2), obtaining the tracer field at $z_{\rm high}$. The iterative process is detailed in the Algorithm (1). From the density field of $\mathbf{q}'$ at each iteration, the power spectrum can be retrieved to check for convergence. Finally, the reconstructed position of the tracer in real space is $\mathbf{q}$ while $\mathbf{qs}$ is the reconstructed position in the redshift space. It is important to note that the reconstructed field in redshift space keeps the contribution of the peculiar velocity field, something fundamental in order to obtain ARF.

In this case, the tracers are galaxies evolved up to a redshift $z_{\rm low} = 0.3$ (§3), and the chosen redshift to perform the reconstruction is $z_{\rm high} = 3$. For the Gaussian filter, the smoothing radius is set to two mesh cells, i.e. $R = 3.9$ Mpc h^{-1}, following a rule of thumb of the mesh cell being $\sim 2-4$ times smaller than the smoothing radius[14]. Finally, the number of iterations was set to three as the size and resolution of the simulation led to a considerable computational time per iteration. Nevertheless, the convergence is sufficiently good at the third iteration as can be checked in the figure 4.1. The reconstruction was performed on both of the paired simulations. The bias post reconstruction can be evaluated in two forms, as in equation (3.5) meaning that $z = z_{\rm low}$ is assumed, and assuming $z = z_{\rm high}$ meaning that the matter power spectrum in equation (3.5) should be scaled to $z = z_{\rm high}$ by the corresponding growth functions , i.e. following equation (2.35). The obtained biases are

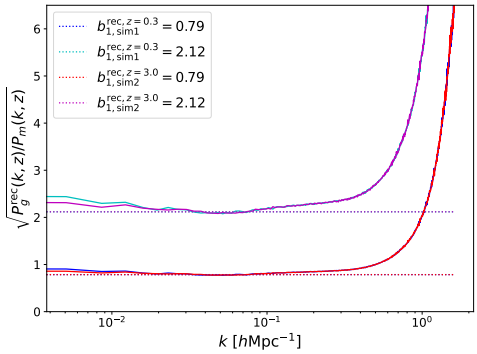

Figure 4.2: Square root of the ratio between tracer and matter power spectrum after reconstruction. The same range for the bias estimate as in figure 3.3 is applicable. Note that the matter power spectrum is scaled to z_{high} for the $b_1^{\mathrm{rec}}(z_{\mathrm{high}})$ estimate.

$$b_1^{\mathrm{rec}}(z_{\mathrm{low}}) = \sqrt{\left\langle \left. \frac{P_g^{\mathrm{rec}}(k)}{P(k)} \right|_{\mathrm{low}\,k} \right\rangle} \Rightarrow b_{1,\mathrm{sim}\,1}^{\mathrm{rec}}(z_{\mathrm{low}}) = b_{1,\mathrm{sim}\,2}^{\mathrm{rec}}(z_{\mathrm{low}}) = 0.79, \tag{4.5}$$

$$b_1^{\mathrm{rec}}(z_{\mathrm{high}}) = \sqrt{\left\langle \left. \frac{P_g^{\mathrm{rec}}(k)}{P(k,z_{\mathrm{high}})} \right|_{\mathrm{low}\,k} \right\rangle} = \sqrt{\left\langle \left. \frac{P_g^{\mathrm{rec}}(k)D^2(z_{\mathrm{low}})}{P(k)D^2(z_{\mathrm{high}})} \right|_{\mathrm{low}\,k} \right\rangle} \tag{4.6}$$

$$\Rightarrow b_{1,\mathrm{sim}\,1}^{\mathrm{rec}}(z_{\mathrm{high}}) = b_{1,\mathrm{sim}\,2}^{\mathrm{rec}}(z_{\mathrm{high}}) = 2.12. \tag{4.7}$$

As done in the catalogues generation §3, the range of k ensuring a good bias estimation should be verified. This is shown in figure 4.2, demonstrating that the same range $0.03 \leq k \leq 0.09$ keeps being applicable.

4.2 Reconstruction Tests

Once the reconstruction up to z_{high} is performed, the first step to test whether its implementation was correct is to inspect the resulting density field and power spectrum. In particular, it is expected to have a more uniform and homogeneous field since the clustering is deconstructed. This is clearly seen in figure 4.3, with a configuration that appears more random and the structures seen pre-reconstruction, less prominent. This is also evident in the power spectrum showing less power at every scale, for both real and redshift spaces. One interesting aspect to note on these power spectra is the higher enhancement of the power spectrum from RSDs after the reconstruction in comparison to the prior enhancement. In the pre reconstruction case, this enhancement is of $\sim 16\%$ while after reconstruction it is $\sim 25\%$ This implies that the tracers become more sensible to RSDs at a reconstructed epoch, something appealing for ARF determination since it would mean a stronger signal.

It also helps to analyze the distribution of the galaxy density field by means of a histogram before and after the reconstruction. Particularly, it is expected that reconstruction gaussianizes the distribution as underdense regions gets populated by the reconstruction process, this is clearly seen in figure 4.4.

Nevertheless, these tests are just qualitative and far from accurate. A quantitative test can be performed in terms of the bias. Particularly, following conservation in the number of tracers, the bias follows a passive evolution described by [11,27–29]

$$b_1(z') = (b_1(z) - 1)\frac{D(z)}{D(z')} + 1, \tag{4.8}$$

allowing to translate a bias at some redshift, e.g. $b_1(z_{\text{low}})$, into a bias at a higher redshift, e.g. $b_1^{\text{rec}}(z_{\text{high}})$. Therefore, an expected value for $b_1^{\text{rec}}(z_{\text{high}})$ can be calculated from the bias pre-reconstruction. Plugging in the calculated bias before the reconstruction $b_{1,\text{sim}\,1} = b_{1,\text{sim}\,1} = 1.32$, leads to a expected value of $b_1^{\text{rec}}(z_{\text{high}}) = 1.87$. The value obtained for the catalogues after the reconstruction is $b_{1,\text{sim}\,1}^{\text{rec}}(z_{\text{high}}) = b_{1,\text{sim}\,2}^{\text{rec}}(z_{\text{high}}) = 2.12$, therefore having a $\sim 13\%$ difference.

Furthermore, an equation to have an expected value for $b_1^{\text{rec}}(z_{\text{low}})$ can also be derived. Noting that the matter power spectrum is equal to the linear one at low k, i.e. $P(k) = P_L(k)|_{\text{low}\,k}$, for a given z the post reconstruction power spectrum is

$$P_g^{\text{rec}}(k) = b_1^{\text{rec}}(z)D^2(z)P_L(k, z = 0)|_{\text{low}\,k}. \tag{4.9}$$

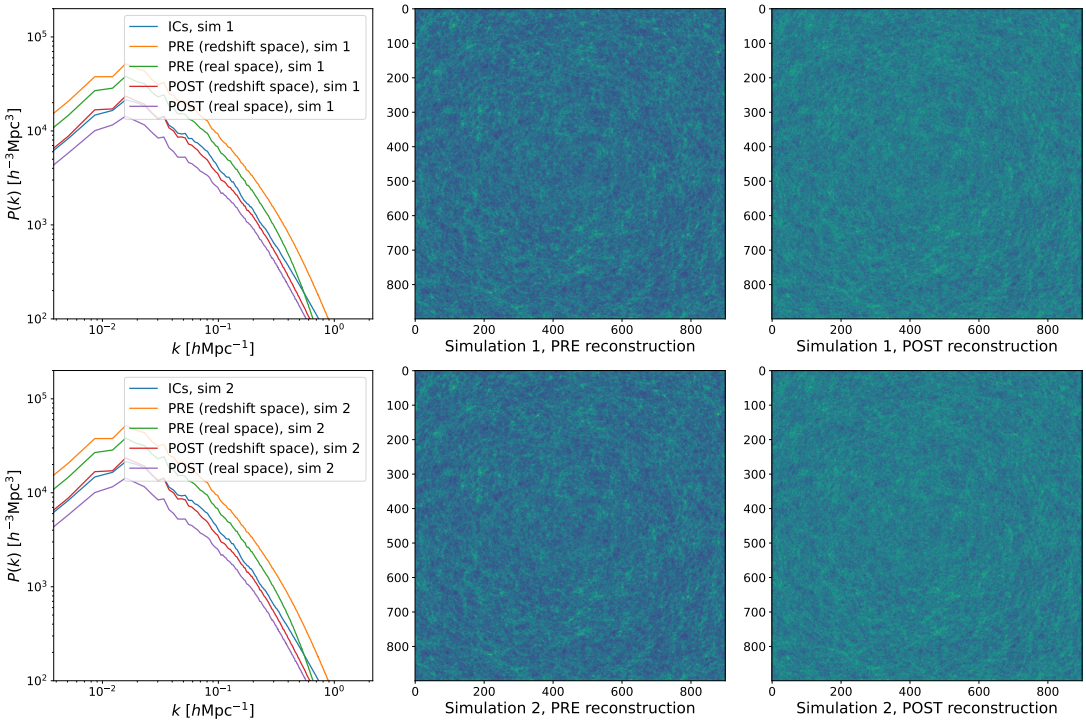

Figure 4.3: Halos power spectrum and density fields before and after the reconstruction process. Note that the density field correspond to redshift space.

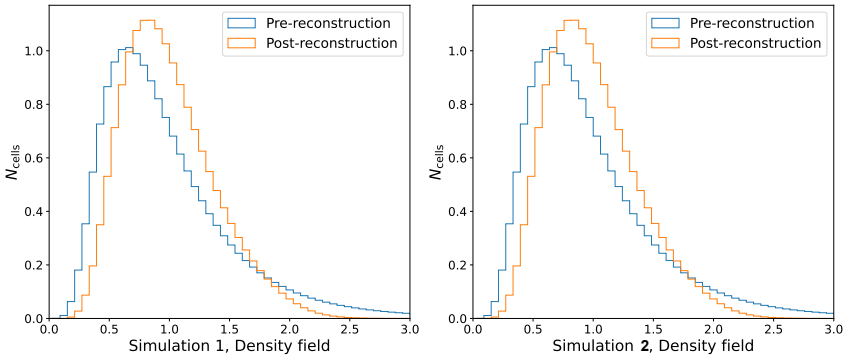

Figure 4.4: Histogram representation of density fields before and after reconstruction. Note the Gaussianization of the distribution with the reconstruction.

Then, having z_{high} and z_{low} implies that $b_1^{\text{rec}}(z_{\text{high}})D(z_{\text{high}}) = b_1^{\text{rec}}(z_{\text{low}})D(z_{\text{high}})$. Plugging this into equation (4.8) leads to

$$b_1^{\text{rec}}(z_{\text{low}}) = b_1(z_{\text{low}}) - 1 + \frac{D(z_{\text{high}})}{D(z_{\text{low}})}. \tag{4.10}$$

Which, for $b_1 = 1.26$,leads to a expected value of $b_1^{\text{rec}}(z_{\text{low}}) = 0.70$. In this case, the value obtained for the catalogues after the reconstruction is $b_{1,\text{sim}\,1}^{\text{rec}}(z_{\text{high}}) = b_{1,\text{sim}\,2}^{\text{rec}}(z_{\text{high}}) = 2.12$, again denoting a $\sim 13\%$ difference.

This apparent difference between the expected and obtained bias values after reconstruction comes from estimating the matter density field from the galaxy field. Since the displacement field is defined from the matter density field, this brings an inevitable level on inaccuracy of the displacement field. Indeed, if the same reconstruction is performed but calculating the true displacement field from the generated matter catalogues, a more consistent result is obtained. Specifically, the obtained values from this test are $b_1^{\text{rec}}(z_{\text{high}}) = 1.94$ and $b_1^{\text{rec}}(z_{\text{low}}) = 0.72$, differing now by only $\sim 3\%$. Therefore, the reconstruction approach demonstrates to be correct, leading to the desired values of two point statistics.

5. ARF & ADF Angular Power Spectrum

After the reconstruction is implemented and validated ARF and ADF can be extracted from the paired simulations. This is done for the two stages, before and after the reconstruction. The reason is that it would allow to compare and determine whether the reconstruction implementation enhances the contribution from RSDs, i.e. the peculiar velocity field, to the ARF. It is important to note that it is at this stage that the the advantage coming from the paired simulations is taken into account in order to suppress the effect of cosmic variance in the ARF and ADF determination. In addition, theoretical ARF and ADF can be computed from theoretic numerical models, allowing to compare and further test the method. Particularly, the ARF and ADF angular power spectrum C_ℓ from the paired simulations, i.e. the average from both simulations, is compared to the theoretical power spectrum to test how well the data fit the model for the same set of parameters. The set of parameters comprises the specific cosmology parameters and the bias.

The observer was placed in the center of the catalogues box. Then, from the box size and cosmology used, the comoving distance to the boundaries corresponds to a redshift of ~ 0.3, defining the central redshift for the Gaussian kernel to evaluate ARF and ADF. The redshift width for the kernel is set to $\sigma_z = 0.01$. The model used to obtain the theoretical power spectrum is one modified from the CAMB [9] linear evolution model to calculate ARF. The model is described in Lima-Hernández *et al.* [30].

The obtained power spectra, before and after the reconstruction, and their respective theoretical counterpart are shown in the figure 5.1. Several things can be noted out from these results. First of all, there is a direct correspondence between the theoretic C_ℓ and the one coming from the simulations in the case before and after the reconstruction, denoting that the properties of the catalogues are consistent with the theory, and that the effective bias is well determined.It is worth to note that the effective bias describing the C_ℓ in this case corresponds to the comoving redshift, i.e. $b_{1,\mathrm{rec}}(z_{\mathrm{obs}})$, defined by the observer position although the catalogue is in a previous epoch, i.e. at z_{rec}. In fact, although the passive evolution increases the bias with respect to a higher redshift, the opposite happens if the evolution is respect to the same redshift. Therefore, the effective bias is lowered (in this case from 1.32 to 0.72, taking the bias calculated from the reconstruction performed with the displacement field mapped from the matter field) making the

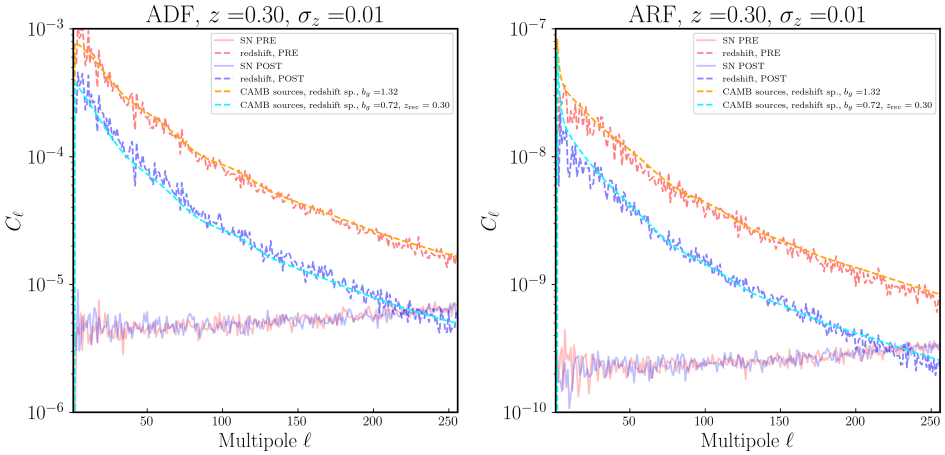

Figure 5.1: Angular power spectrum C_ℓ from ARF and ADF. The curves correspond to the C_ℓ before and after reconstruction as well as the theoretic C_ℓ computed from CAMB models for the simulation parameters. Curves denoting the shot noise (SN) are also included.

post reconstruction catalogue more sensible to the peculiar velocities. Particularly, unravelling gravity linearizes the field making it more sensible to RSDs. In fact, noting that the RSD factor is $\beta = f/b_1$, given that the bias decreases, the factor increases. This fact is fundamental and demonstrates the feasibility of combining reconstruction techniques with ARF and ADF. Actually, the contribution of velocity terms to the C_ℓ amplitude can be evaluated. Particularly, the ratio $(C_\ell - C_\ell^{\text{real space}})/C_\ell$ is sensible to the relative contribution of the velocity terms, and thus to $f(z)\sigma_8(z)$, to the ADF and ARF power spectra. The estimated ratio from the modified linear CAMB model[30] for the set of obtained parameters is shown in the figure 5.2. Particularly it can be seen that the ARF contain more power sensible to the peculiar velocites than the ADF. Additionally, reconstruction enhances the contribution of the terms generated from the peculiar velocities. Therefore, not only the tracer field is more sensible to peculiar velocities after reconstruction was applied but also ARF and ADF are more sensible, demonstrating the validity of applying reconstruction to improve the applicability of ARF and ADF.

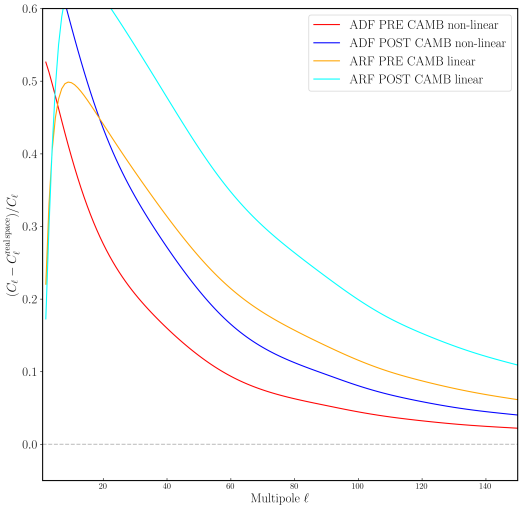

Figure 5.2: Ratio of the angular power spectrum showing the sensibility of ARF and ADF to the relative contribution of peculiar velocity terms.

6. Conclusions & Outlook

In this work a combination of methods, cosmological reconstruction with ARF and ADF determination, was proposed and tested. Particularly, ARF and ADF are robust observables that nevertheless suffer from being limited to bigger scales. Therefore, cosmological reconstruction, taking an evolved epoch of the universe to a previous epoch, surges as a natural way to improve the applicability of these observables. This was put to test on mock catalogues that were simulated from two paired initial conditions so that the final results are not affected by cosmic variance. The catalogues were evolved up to a redshift $z = 0.3$ and the reconstruction took these catalogues to a higher redshift of $z = 3.0$.

Reconstruction showed to lower the bias of the catalogues with respect to the same comoving redshift. This leads to the reconstructed field being more sensible to RSDs, which is evident by comparing the power spectrum of the reconstructed field in redshift and real space. Additionally, the obtained ARF and ADF power spectrum showed to be consistent with theoretical models for the same set of parameters, implying the correctness of their determination and the higher sensibility to RSDs after the reconstruction.

From the reconstructed field being more sensible con RSDs, it follows that ARF and ADF become also more sensible to the peculiar velocity field. This represents the main conclusion of this study, in fact, the peculiar velocity term of the ARF and ADF power spectra has a higher contribution to the C_ℓ amplitude as was demonstrated from the $(C_\ell - C_\ell^{\text{real space}})/C_\ell$ ratio, which is sensible to $f(z)\sigma_8(z)$. Accordingly, this demonstrates the feasibility of combining reconstruction techniques with ARF and ADF determination. In fact, objects with a high bias, i.e. $b_1 > 1$, could have had lowered their bias up to and even bellow ~ 1 by reconstruction allowing for a better determination of cosmological parameters through ARF and ADF.

Finally, it is worth to state that in the constructed catalogues for this study, the RSDs are only due to coherent peculiar velocity leading to the squashing effect. A more complete approach would be to start from a catalogue including the dispersed component of the peculiar velocity, leading to the Fingers-of-God effect and later apply a more robust reconstruction approach, such as COSMIC BIRTH[24], implementing a higher order sampling of the displacement field. This would allow to better test the contribution of peculiar velocities to ARF and ADF in a more

realistic approach, and potentially improve the correspondence of the C_ℓ post reconstruction to the theory, from a more accurate mapping of the displacement field. Additionally, a natural step is to further test the method at higher redshifts and real survey data. And ultimately, to combine the techniques on the potential aplications of ARF and ADF observables, e.g. tomographic tests of observables with theoretical predictions or constrains in cosmological parameters.

A. Linearization of Newtonian fluids equations.

To start, recall the transformations in equations (2.19) and (2.20) to be implemented of the set of equations (2.16), (2.17), and (2.18). Additionally, a perturbation over the smooth background is applied in the form of $\rho = \rho_0(1+\delta)$ ($\delta = \delta_\rho/\rho_0$), $P = P_0 + \delta_P$, and $\Phi = \Phi_0 + \delta_\Phi$.

Taking first the continuity equation (2.16) and plugging these changes:

$$\left(\frac{d}{dt} + \mathbf{u}\cdot\nabla\right)\rho_0(1+\delta) = -\rho_0(1+\delta)\nabla_r\cdot(H\mathbf{r} + a\mathbf{u}),$$
$$(1+\delta)\frac{d\rho_0}{dt} + \rho_0\frac{d\delta}{dt} + \rho_0(\mathbf{u}\cdot\nabla)\delta = -\rho_0(1+\delta)(3H + \nabla\cdot\mathbf{u}),$$

where $(\mathbf{u}\cdot\nabla)\rho_0 = 0$ was applied (from isotropy and homogeneity), and $\nabla_r\cdot(H\mathbf{r}) = 3H$. Additionally, noting that $\rho_0 \propto a^{-3} \rightarrow \rho_0 = \rho(0)a^{-3}$ and therefore $\frac{d\rho_0}{dt} = -3\rho(0)a^{-4}\dot{a} = -3H\rho_0$, the equation becomes

$$\frac{d\delta}{dt} = -(1+\delta)\nabla\cdot\mathbf{u} - (\mathbf{u}\cdot\nabla)\delta \xRightarrow{\text{1st order terms}} \frac{d\delta}{dt} = -\nabla\cdot\mathbf{u}.$$

and the linearized continuity equation (2.21) was obtained by keeping first order terms only.

Following the same process for the Euler equation (2.17) leads to

$$\frac{d\mathbf{v}}{dt} + (\mathbf{u}\cdot\nabla)\mathbf{v} = -\frac{\nabla_r P}{\rho} - \nabla_r\Phi$$
$$\frac{d}{dt}(H\mathbf{r} + a\mathbf{u}) + (\mathbf{u}\cdot\nabla)H\mathbf{r} + (\mathbf{u}\cdot\nabla)a\mathbf{u} = -\frac{1}{a}\frac{\nabla(P_0+\delta_P)}{\rho_0(1+\delta)} - \frac{1}{a}\nabla(\Phi_0+\delta_\Phi)$$
$$\frac{dH\mathbf{r}}{dt} + \dot{a}\mathbf{u} + a\frac{d\mathbf{u}}{dt} + a\mathbf{u}H + (\mathbf{u}\cdot\nabla)a\mathbf{u} \simeq -\frac{1}{a}\frac{\nabla(P_0+\delta_P)}{\rho_0}(1-\delta) - \frac{1}{a}\nabla\Phi_0 - \frac{1}{a}\nabla\delta_\Phi$$
$$\simeq -\frac{1}{a}\frac{\nabla P_0}{\rho_0} + \frac{\delta_\rho}{a}\frac{\nabla P_0}{\rho_0^2} - \frac{1}{a}\frac{\nabla\delta_P}{\rho_0} + \frac{\delta}{a}\frac{\nabla\delta_P}{\rho_0} - \frac{1}{a}\nabla\Phi_0 - \frac{1}{a}\nabla\delta_\Phi,$$

where the term $(\mathbf{u}\cdot\nabla)H\mathbf{r}$ is $[u]_i a[\nabla_r]_i H[r]_j = aH[u]_i\delta_{ij} = aH\mathbf{u}$, and the first term in the r.h.s. was approximated by a first order Taylor expansion. Recalling that the zeroth order Euler equation

is $\frac{dH\mathbf{r}}{dt} = -\frac{1}{a}\frac{\nabla P_0}{\rho_0} - \frac{1}{a}\nabla\Phi_0$, and dropping second order and negligible terms leads to the linearized Euler equation (2.22)

$$a\frac{d\mathbf{u}}{dt} + 2\dot{a}\mathbf{u} = -\frac{1}{a}\frac{\nabla\delta_P}{\rho_0} - \frac{1}{a}\nabla\delta_\Phi \Rightarrow \frac{d\mathbf{u}}{dt} + 2H\mathbf{u} = -\frac{1}{a^2}\frac{\nabla\delta_P}{\rho_0} - \frac{1}{a^2}\nabla\delta_\Phi.$$

In the case of the Poisson equation (2.18), the process to its linearized equation (2.23) is straightforward

$$\begin{aligned}\nabla_r^2(\Phi_0 + \delta_\Phi) = \frac{1}{a^2}\nabla^2\Phi_0 + \frac{1}{a^2}\nabla^2\delta_\Phi &= 4\pi G\rho_0(1+\delta)\\ \Rightarrow \nabla^2\delta_\Phi &= 4\pi a^2 G\rho_0\delta,\end{aligned}$$

where the cancelled terms are due to the zeroth order equation.

Analyzing the peculiar velocity, $\mathbf{u}$, from the linearized Euler equation (2.21) it can be separated the parallel and perpendicular components, with respect to $\nabla\Phi$. Then $\mathbf{u} = \mathbf{u}_\parallel + \mathbf{u}_\perp$, particularly the perpendicular component of equation (2.22) being

$$\frac{d\mathbf{u}_\perp}{dt} + 2H\mathbf{u}_\perp = 0 \Rightarrow \mathbf{u}_\perp \propto a^{-2}, \delta_{\mathbf{v},\perp} \propto a^{-1},$$

meaning that it decays leading to the primordial vorticity getting erased, i.e. the peculiar velocity today is expected to be curl-free.

Now, looking for a solution of the peculiar velocity of the form $\mathbf{u} = -F(t)\frac{\nabla\delta_\Phi}{a} = F(t)\mathbf{g}$, with $\mathbf{g} = -\frac{\nabla\delta_\Phi}{a}$ the peculiar gravitational acceleration, from equation (2.21) it follows that

$$\frac{d\delta}{dt} = -\nabla\cdot\mathbf{u} = F(t)\frac{\nabla^2\delta_\Phi}{a} = F(t)4\pi G a\rho_0\delta.$$

Where equation 2.23 was used. Plugging in the Friedmann equation at critical density, i.e. equation (2.6), $H^2 = \frac{8\pi G\rho}{3\Omega}$, and solving for $F(t)$:

$$F(t) = \frac{d\delta}{dt}\frac{2}{3H^2\Omega a\delta} = \frac{2}{3H^2\Omega a\delta}\frac{d\delta}{da}\frac{da}{dt} = \frac{2}{3H\Omega}\frac{d\delta/da}{\delta}.$$

Then, defining $f(\Omega) = \frac{a}{\delta}\frac{d\delta}{da}$, the peculiar velocity is

$$\delta_\mathbf{v} = a\mathbf{u} = aF(t)\mathbf{g} = \frac{2f(\Omega)}{3H\Omega}\mathbf{g}.$$

Alternatively, in Fourier terms, having $\delta_\Phi = \delta_{\Phi,\mathbf{k}} \exp(-i\mathbf{k}\cdot\mathbf{x})$ and $\delta = \delta_\mathbf{k} \exp(-i\mathbf{k}\cdot\mathbf{x})$ then equation (2.23) is $-\frac{k^2}{a^2}\delta_{\Phi,\mathbf{k}} = 4\pi G\rho_0\delta_\mathbf{k}$ and the peculiar gravity becomes

$$\mathbf{g} = -\frac{\nabla\delta_\Phi}{a} = i\mathbf{k}\frac{\delta_{\Phi,\mathbf{k}}}{a}\exp(-i\mathbf{k}\cdot\mathbf{x}) = -i\frac{\mathbf{k}}{k^2}4\pi G\rho_0 a\delta_\mathbf{k}\exp(-\mathbf{k}\cdot\mathbf{x}) \Rightarrow \mathbf{g} = -i\frac{\mathbf{k}}{k^2}\frac{3H^2\Omega a}{2}\delta,$$

to finally have

$$\delta_\mathbf{v} = -i\frac{\mathbf{k}}{k^2}faH\delta.$$

Bibliography

[1] Weinberg, D. H.; Mortonson, M. J.; Eisenstein, D. J.; Hirata, C.; Riess, A. G.; Rozo, E. Observational probes of cosmic acceleration. *PhR* **2013**, *530*, 87–255.

[2] Planck Collaboration, *et al.* Planck 2015 results. XIII. Cosmological parameters. *A&A* **2016**, *594*, A13.

[3] Guth, A. H. Inflationary universe: A possible solution to the horizon and flatness problems. *Phys. Rev. D* **1981**, *23*, 347–356.

[4] Linde, A. A new inflationary universe scenario: A possible solution of the horizon, flatness, homogeneity, isotropy and primordial monopole problems. *Physics Letters B* **1982**, *108*, 389–393.

[5] Peacock, J. A. *Cosmological Physics*; 1999.

[6] Peebles, P. J. E. *The large-scale structure of the universe*; 1980.

[7] Zel'dovich, Y. B. Gravitational instability: An approximate theory for large density perturbations. *A&A* **1970**, *5*, 84–89.

[8] Eisenstein, D. J.; Hu, W.; Tegmark, M. Cosmic Complementarity: H_0 and Ω_m from Combining Cosmic Microwave Background Experiments and Redshift Surveys. *ApJ* **1998**, *504*, L57–L60.

[9] Lewis, A.; Challinor, A.; Lasenby, A. Efficient Computation of Cosmic Microwave Background Anisotropies in Closed Friedmann-Robertson-Walker Models. *ApJ* **2000**, *538*, 473–476.

[10] Lesgourgues, J. The Cosmic Linear Anisotropy Solving System (CLASS) I: Overview. *arXiv e-prints* **2011**, arXiv:1104.2932.

[11] Fry, J. N. The Evolution of Bias. *ApJL* **1996**, *461*, L65.

[12] Kaiser, N. Clustering in real space and in redshift space. *MNRAS* **1987**, *227*, 1–21.

[13] Hernández-Monteagudo, C.; Chaves-Montero, J.; Angulo, R. E. Density weighted angular redshift fluctuations: a new cosmological observable. *MNRAS* **2021**, *503*, L56–L61.

[14] Hand, N.; Feng, Y.; Beutler, F.; Li, Y.; Modi, C.; Seljak, U.; Slepian, Z. nbodykit: An Open-source, Massively Parallel Toolkit for Large-scale Structure. *AJ* **2018**, *156*, 160.

[15] Angulo, R. E.; Pontzen, A. Cosmological N-body simulations with suppressed variance. *MNRAS* **2016**, *462*, L1–L5.

[16] Chuang, C.-H.; Kitaura, F.-S.; Prada, F.; Zhao, C.; Yepes, G. EZmocks: extending the Zel'dovich approximation to generate mock galaxy catalogues with accurate clustering statistics. *MNRAS* **2015**, *446*, 2621–2628.

[17] Press, W. H.; Schechter, P. Formation of Galaxies and Clusters of Galaxies by Self-Similar Gravitational Condensation. *ApJ* **1974**, *187*, 425–438.

[18] Peacock, J. A.; Heavens, A. F. The statistics of maxima in primordial density perturbations. *MNRAS* **1985**, *217*, 805–820.

[19] Kitaura, F. S.; Yepes, G.; Prada, F. Modelling baryon acoustic oscillations with perturbation theory and stochastic halo biasing. *MNRAS* **2014**, *439*, L21–L25.

[20] Padmanabhan, N.; Xu, X.; Eisenstein, D. J.; Scalzo, R.; Cuesta, A. J.; Mehta, K. T.; Kazin, E. A 2 per cent distance to z = 0.35 by reconstructing baryon acoustic oscillations - I. Methods and application to the Sloan Digital Sky Survey. *MNRAS* **2012**, *427*, 2132–2145.

[21] Zhai, Z.; Wang, Y.; Benson, A.; Chuang, C.-H.; Yepes, G. Linear bias and halo occupation distribution of emission-line galaxies from Nancy Grace Roman Space Telescope. *MNRAS* **2021**, *505*, 2784–2800.

[22] Eisenstein, D. J.; Seo, H.-J.; White, M. On the Robustness of the Acoustic Scale in the Low-Redshift Clustering of Matter. *ApJ* **2007**, *664*, 660–674.

[23] Eisenstein, D. J.; Seo, H.-J.; Sirko, E.; Spergel, D. N. Improving Cosmological Distance Measurements by Reconstruction of the Baryon Acoustic Peak. *ApJ* **2007**, *664*, 675–679.

[24] Kitaura, F.-S.; Ata, M.; Rodríguez-Torres, S. A.; Hernández-Sánchez, M.; Balaguera-Antolínez, A.; Yepes, G. COSMIC BIRTH: efficient Bayesian inference of the evolving cosmic web from galaxy surveys. *MNRAS* **2021**, *502*, 3456–3475.

[25] Kitaura, F.-S.; Ata, M.; Angulo, R. E.; Chuang, C.-H.; Rodríguez-Torres, S.; Monteagudo, C. H.; Prada, F.; Yepes, G. Bayesian redshift-space distortions correction from galaxy redshift surveys. *MNRAS* **2016**, *457*, L113–L117.

[26] Hada, R.; Eisenstein, D. J. Application of the iterative reconstruction to simulated galaxy fields. *MNRAS* **2019**, *482*, 5685–5693.

[27] Nusser, A.; Davis, M. On the Prediction of Velocity Fields from Redshift Space Galaxy Samples. *ApJL* **1994**, *421*, L1.

[28] Hamilton, A. J. S. In *The Evolving Universe: Selected Topics on Large-Scale Structure and on the Properties of Galaxies*; Hamilton, D., Ed.; Springer Netherlands: Dordrecht, 1998; pp 185–275.

[29] Percival, W. J.; Schäfer, B. M. Galaxy peculiar velocities and evolution-bias. *MNRAS* **2008**, *385*, L78–L82.

[30] Lima-Hernández, A.; Hernández-Monteagudo, C.; Chaves-Montero, J. Relativistic Angular Redshift Fluctuations embedded in Large Scale Varying Gravitational Potentials. *arXiv e-prints* **2022**, arXiv:2203.15008.